



Cite this: DOI: 10.1039/d0lc00951b

## Biological gel-based microchamber array for tumor cell proliferation and migration studies in well-controlled biochemical gradients†

Jingru Yao,<sup>‡,a</sup> Guoqiang Li,<sup>‡,a</sup> Yang Jiao,<sup>b</sup> Yu Zheng,<sup>b</sup> Yanping Liu,<sup>a</sup> Gao Wang,<sup>a</sup> Lianjie Zhou,<sup>a</sup> Hongfei Zhang,<sup>c</sup> Xianquan Zhang,<sup>c</sup> Jianwei Shuai,<sup>de</sup> Qihui Fan,<sup>d</sup> Fangfu Ye,<sup>ef</sup> Silong Lou,<sup>g</sup> Guo Chen,<sup>a</sup> Kena Song,<sup>\*ah</sup> Yong Liao,<sup>\*i</sup> and Liyu Liu <sup>iD, \*a</sup>

Breast cancer metastasis is a complex process controlled by multiple factors, including various cell-cell interactions, cell–environment coupling, and oxygen, nutrient and drug gradients that are intimately related to the heterogeneous breast tissue structure. In this study, we constructed a high-throughput *in vitro* biochip system containing an array of 642 microchambers arranged in a checkerboard configuration, with each chamber embedded in a composite extracellular matrix (ECM) composed of engineered collagen and Matrigel to mimic local heterogeneous environment *in vivo*. In addition, a controllable complex tetragonal chemical concentration profile can be achieved by imposing chemical compounds at the four boundaries of the chip, leading to distinct local nutrient and/or drug gradients in the individual microchambers. Here, the microchamber array with composite ECM (MACECM) device aims to simulate multiple tumor cell niches composed of both breast epithelial cells (MCF-10A-GFP) and metastatic breast cancer cells (MDA-MB-231-RFP), which enables systematic studies of cell responses to a variety of biochemical conditions. The results obtained from the MACECM studies indicate that discoidin domain receptor 1 (DDR1) inhibitor 7rh and matrix metalloproteinase inhibitor batimastat, in association with epidermal growth factor (EGF) had no significant effects on the growth of MCF-10A-GFP cells, but had significant effects on DDR1 expression and the related migratory behavior of MDA-MB-231-RFP cells. The MACECM design not only enables the construction of a more realistic *in vitro* model for investigating cancer cell migration mechanisms but also has considerable potential for further development as a platform for next-generation high-throughput and therapeutic screening (e.g., anti-cancer drug evaluation) and personalized medicine.

Received 21st September 2020,  
Accepted 28th May 2021

DOI: 10.1039/d0lc00951b

rsc.li/loc

<sup>a</sup> Chongqing Key Laboratory of Soft Condensed Matter Physics and Smart Materials, College of Physics, Chongqing University, Chongqing 401331, China. E-mail: lyliu@cqu.edu.cn

<sup>b</sup> Materials Science and Engineering, Arizona State University, Tempe, Arizona, 85281, USA

<sup>c</sup> Hygeia International Cancer Hospital, Chongqing 401331, China

<sup>d</sup> Department of Physics, Xiamen University, Xiamen 361005, China

<sup>e</sup> Wenzhou Institute, University of Chinese Academy of Sciences, Wenzhou, 325000, China

<sup>f</sup> Beijing National Laboratory for Condensed Matter Physics, Institute of Physics, Chinese Academy of Sciences, Beijing 100190, China

<sup>g</sup> Chongqing University Cancer Hospital, Chongqing 400044, China

<sup>h</sup> College of Medical Technology and Engineering, Henan University of Science and Technology, Henan 471023, China. E-mail: kenasong@cqu.edu.cn

<sup>i</sup> Institute for Viral Hepatitis, Department of Infectious Diseases, Second Affiliated Hospital, Chongqing Medical University, Chongqing 400331, China. E-mail: yongliao@cqmu.edu.cn

† Electronic supplementary information (ESI) available. See DOI: 10.1039/d0lc00951b

‡ J. Y. and G. L. contributed equally to this work.

## Introduction

Breast cancer is a malignant disease and a serious threat to women's health.<sup>1,2</sup> Our understanding of tumor development at the proteogenomics and molecular levels and clinical treatment strategies for patients with breast cancer have improved drastically in the past two decades,<sup>3</sup> but still the outcome for many patients with metastatic breast cancer remains fatal. Taking advantage of the unique breast tissue architecture, breast cancer can develop both local invasion and remote metastasis, which is the underlying cause of death in the majority of breast cancer patients.<sup>4,5</sup> The tumor microenvironment, especially the extracellular matrix (ECM), plays an essential role in breast tumor cell invasion and migration.<sup>6,7</sup> An important question to address for better understanding of breast cancer metastasis is how the local heterogeneous microenvironment affects the migration of tumor cells during the early stages.

Fig. 1A schematically illustrates the complex breast tissue structure. When invasive ductal carcinoma occurs, tumor

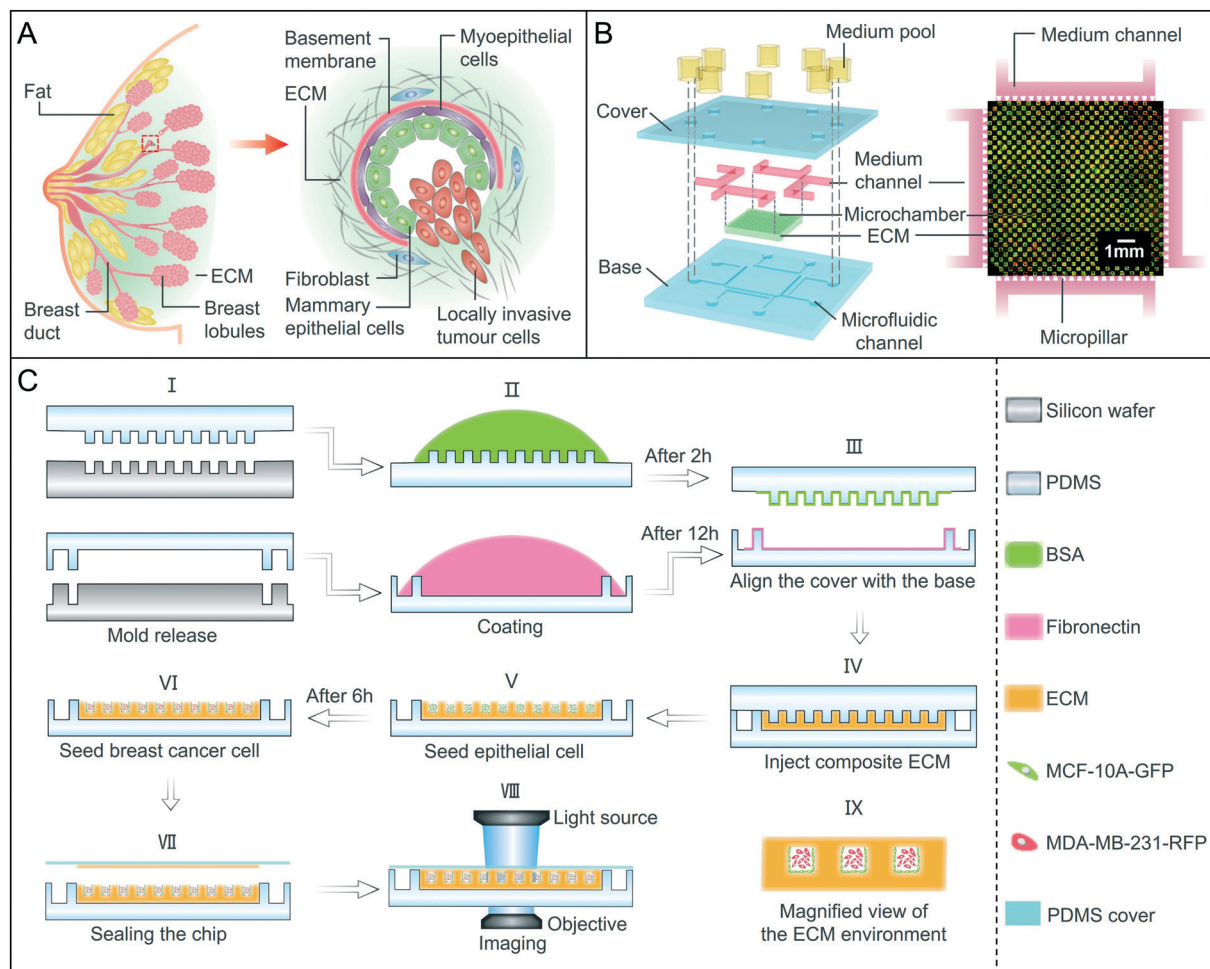


**Fig. 1** Breast invasive ductal carcinoma and MACECM chip design. (A) Illustration of breast duct carcinoma invasion and metastasis. (B) The design of the biochip and its microchamber array. The left inset shows the chip-layered structures. The right inset shows the amplified pictures of the ECM region and tetragonal microfluidic channels. The microchamber array have mcf-10a-gfp cells (green) and mda-mb-231-rfp cells (red) cultured inside and are surrounded by the ECM (black). (C) MACECM chip design and fabrication procedures. (I) The ECM mould (blue, above) and the chip base (blue, below) are obtained via soft lithography. (II) The mould and the base surface are modified with BSA (green) and fibronectin (red). (III) Assembling the two components. (IV) ECM (orange) injection inside the chamber. (V) MCF-10A-GFP (green) culture and cell niche structure formation. (VI) After 6.0 h, the MDA-MB-231-RFP (red) cells were introduced. (VII) Chip sealing by the PDMS cover. (VIII) Microscopy of the cancer cell niche structures and cell development. (IX) The amplified array structures indicate that the cancer cell niche structures are completely wrapped by the ECM.

cells (red) interact with mammary epithelial cells (green) and myoepithelial cells (purple), break through the basement membrane (pink) and migrate outside the ductal structure. The escaped tumor cells subsequently encounter the ECM, which typically contains several components, such as collagen fibers (grey), fibroblast cells (blue), etc. Moreover, oriented fiber bundles can greatly enhance breast tumor cell invasion and migration.<sup>8,9</sup> Besides interacting with various cells and structures from duct to stroma, breast tumor cells also experience complex biochemical microenvironments such as various growth factors and drugs. The physical and biochemical coupling mechanisms determine cell invasion and subsequent metastasis. However, to the best of our knowledge, the coupling mechanisms and their influence on cancer cell invasion and metastasis, which are typically investigated and revealed via carefully designed *in vitro*

experiments, still largely remain unclear. The major challenge for such *in vitro* studies involves reconstructing a realistic tumor microenvironment mimicking the physical microstructures and heterogeneities of breast tissue and the establishment of a complex biochemical environment that are representatives of the *in vivo* situation.

It is generally very challenging and extremely difficult to realistically mimic the *in vivo* cell microenvironment, particularly localized cell niches with related functions, using *in vitro* technology. Nonetheless, with an overarching goal to better understand tumor cell invasion and metastasis in complex tissue environments, various experimental models using the lab-on-a-chip or organ-on-a-chip designs have been generated.<sup>10,11</sup> These biochips with complex configurations and functions offer more realistic *in vitro* platforms for the actual *in vivo* environment than the widely used two-

dimensional cell culture on a Petri dish. In addition, the above systems with the advantages of high simulation and controllability allow easy device manipulation, quantification of cell statistics, *etc*. In particular, significant efforts have aimed to develop complex biochips for mimicking breast microstructures and the associated microenvironments. For example, a micro-engineered pathophysiological model has been reported for modelling early-stage breast cancer.<sup>12</sup> Despite the exciting progress, there are still two important features that are missing in the preponderance of previously developed biochip systems and need to be addressed in the *in vitro* breast tumor chip model: (1) incorporation of a more realistic microenvironment composed of ECM and micro niche structures, the co-existence of metastatic cancer cells with endothelial cells, and oriented collagen structure, which better mimic the *in vivo* situation; (2) establishment of a stable and complex biochemical environment mimicking *in vivo* biochemical gradients taking advantage of the ECM structure. Breast tissue itself is rich in nutritional factors, such as epidermal growth factor (EGF), serum and glucose, and when patients receive chemotherapy, more complex biochemical gradient environments are introduced. So far, various gradient generator designs have been applied in cell microenvironment construction. In terms of spatial dimensions, the generators are classified into two-dimensional (2D) and three-dimensional (3D) types. The 2D gradient systems are based on planar space and generate gradients *via* convection or diffusion.<sup>13,14</sup> The 3D gradient systems are based on three-dimensional microenvironments or bionic tissue structures and mostly generate gradients *via* diffusion.<sup>15,16</sup> Compared to 2D systems, gels present more advantages in generating 3D chemical gradients. This is because gel bases are not only able to mimic an *in vivo* microenvironment and provide cells with mechanical support and chemical stimulations but also able to absorb liquid and facilitate diffusion of gas, nutrition, proteins and signaling molecules. However, current gradient generators still face great challenges for cell-related application. In particular, individualized featured designs are required for specific research.

Here, in order to achieve an *in vitro* model for the physical structures and biochemical environment of multiple cancer cell niches in the ECM, we have designed and fabricated a 642 microchamber array embedded in composite ECM (MACECM) integrated as a high-throughput biochip system with composite but stable gradients associated with four biochemicals. It is expected that the designed system is able to provide a stable and unique local biochemical environment for the cells in each chamber. In combination with microscopic real-time imaging techniques, individual cell behavior, such as growth, proliferation and migration can be imaged at the single-cell level for quantitative analysis. This further allows us to systematically investigate and explore the various coupling effects among microenvironments, cells, and chemical factors on breast cancer cell dynamics in a single experiment, with the merits

of saving time and consumable costs while ensuring test accuracy. In addition, the MACECM system possesses significant advantages in identifying and evaluating promising chemical compound candidates for tumor suppression and treatment with ease and precision. With both analysis of cell dynamics and optic characterization of cell biomarkers, we demonstrate that our MACECM device allows one to mimic multiple niches for tumor cells in tissues *in vitro* and quantitatively investigate superposed drugs' effects in a highly efficient manner.

## Experimental methods

### Design and fabrication of MACECM

As illustrated in Fig. 1B, the biochip is structurally composed of four layers: the polydimethylsiloxane (PDMS) base (blue) with a microfluidic channel, the ECM region (green), the medium channel (pink) and PDMS cover (blue). Specifically, the base layer supports four independent microfluidic channels for different media, and the central square region is prepared for loading the ECM and cells. The upper layer is a PDMS cover to seal the biochip with punched holes connected to medium reservoirs (yellow) in the external layer. An inverted microscope (Ti-E, Nikon, Japan) was employed to capture the image of the complete ECM chamber area (Fig. 1B, right). The ECM consists of 642 microchambers in a "checkerboard" array and each chamber contains cultured MCF-10A-GFP cells (green) and MDA-MB-231-RFP cells (red). The tetragonal lined trapezoid pillars (white) have a 40  $\mu$ m gap between each other and separate the central ECM from the four medium channels on the edges. The medium was diffused through the gaps into the ECM and supplied the cells with biochemical compounds.

Fig. 1C shows the detailed fabrication process of the biochip. In step I, two silicon moulds (grey) were prepared *via* standard UV lithography techniques to simultaneously construct an ECM mould (blue) and a PDMS base (blue) *via* soft-lithography. In step II, the mould was wetted with 2.0% bovine serum albumin (BSA, Cell Signaling Technology, USA) (green) for 2.0 h and prevented from sticking to the ECM. The base was incubated by fibronectin (Corning, NY, USA) (pink) for 12.0 h, which enables strong binding to the ECM. In step III, after the mould and the base were surface-covered with BSA and fibronectin, respectively, they were bonded together and formed the middle chambers where composite ECM (orange) was seeded (step IV). After the ECM gel was solidified, the upper mould was peeled off. Then, MCF-10A-GFP cells (green) were injected inside the ECM chambers (step V). In step VI, the MCF-10A-GFP cells stuck to the walls where MDA-MB-231-RFP cells (red) were seeded. In step VII, the PDMS cover (blue) with pre-coated ECM sealed the biochip, which was then placed in a live-cell culture system (Okolab, Italy) for continuous cell culture and microscopic imaging (step VIII). Finally, in step IX, the biochip with high-throughput chambers was constructed for modeling of *in vivo* breast tumor cell niches. The central ECM region

formed a number of structures *via* MCF-10A-GFP cells and inner MDA-MB-231-RFP cells, while the chamber was surrounded by ECM outside.

### Composite ECM preparation

ECM is considered a key component for modelling multiple niches for tumor cell. It not only provides solid and stable physical support for cells but is also necessary for the transportation of medium and other biochemicals. Collagen is one of the most commonly used biocompatible materials for *in vitro* ECM construction. Its network structure enhances tissue diffusion and permeability and is beneficial for cell growth and invasion.<sup>17,18</sup> More importantly, fibrotic collagen is easily shaped into a fiber-oriented microenvironment for cancer cell invasion when applied with controllable stress.<sup>8</sup> However, the weakness of collagen is that it is relatively soft, with a Young's modulus of 100.0 Pa at 2.0 mg mL<sup>-1</sup>, and the structure may easily collapse in long-term experiment.<sup>19,20</sup> Meanwhile, Matrigel is the main component of the basement membrane and is much stiffer with a Young's modulus of 450.0 Pa at 100% concentration.<sup>8</sup> It is not only commonly used as the ECM for epithelial cell and endothelial cell culture *in vitro*<sup>21,22</sup> but is also employed to construct an *in vivo* micro-vessel structure for investigating cancer angiogenesis.<sup>23,24</sup> In our experiment, a mixture of collagen and Matrigel was used to construct the ECM structures inside the biochip. First, collagen I extracted from rat tail (354236, Corning, NY, USA)<sup>25,26</sup> and Matrigel (356237, Corning, NY, USA) at concentrations of 9.5 mg mL<sup>-1</sup> and 20.0 mg mL<sup>-1</sup> were added to PBS (Corning, NY, USA), diluting their concentrations to 6.0 mg mL<sup>-1</sup> and 10.0 mg mL<sup>-1</sup>, respectively. Then, the two gels were mixed at a 1:1 ratio before the mixture was incubated at 37.0 °C for 4 h. The reason for the usage of composite gel is explained later in the Results and discussion.

### Cell culture and seeding

The malignant breast cancer cell line MDA-MB-231-RFP, marked with red fluorescent protein (RFP), and healthy human breast epithelial cell line MCF-10A-GFP, marked with green fluorescent protein (GFP), were obtained from China Infrastructure of Cell Line Resources (Beijing, China). For GFP transfection, lentiviral plasmid (pEGFP) vector mediated GFP gene was integrated into host cell genome, while lentiviral plasmid (PFV) vector mediated RFP gene was integrated into the cells in the same way. Both proteins localized in cell cytoplasm, nucleus, and membrane. MCF-10A-GFP cells were cultured in Dulbecco's modified Eagle medium F12 (DMEM/F12, Corning, NY, USA) supplemented with 5.0% (v/v) horse serum (Gibco, NY, USA), 1.0% (v/v) penicillin/streptomycin (Corning, NY, USA), 20.0 ng mL<sup>-1</sup> human EGF (Gibco, NY, USA), 10.0 µg mL<sup>-1</sup> insulin (Roche Diagnostics GmbH, CH, USA), 100.0 ng mL<sup>-1</sup> cholera toxin (Sigma, MO, USA), and 0.5 µg mL<sup>-1</sup> hydrocortisone (Corning, NY, USA). MDA-MB-231-RFP cells were maintained in DMEM

(Corning, NY, USA) supplemented with 10.0% (v/v) foetal bovine serum (Gibco, NY, USA) and 1.0% (v/v) penicillin/streptomycin (Corning, NY, USA). All cells were cultured in an incubator at 37.0 °C with 5.0% CO<sub>2</sub>. During the experiment, MDA-MB-231-RFP cells and MCF-10A-GFP cells were seeded into the microchambers of the biochip at 5.0 × 10<sup>6</sup> cells per mL, and the medium of the two cells was mixed at a 1:1 ratio for co-culture.

### Immunofluorescence analysis

For the cell immobilization process, PBS (Corning, NY, USA) and 4.0% paraformaldehyde (Beyotime, MA, USA) were preheated to 37.0 °C before the medium was removed from the biochip's reservoir. Then, the reservoir was filled with PBS and allowed to stand for 15.0 min before aspiration. This operation was repeated three times until the previous medium was completely removed. Next, the reservoir was filled with the preheated 4.0% paraformaldehyde and maintained for 40.0 min to fix cells. Finally, the paraformaldehyde was removed and the chip was rinsed with PBS again three times. For immunofluorescence staining, the primary antibody DDR1 (D1G6) XP rabbit mAb (Cell Signalling Technology, MA, USA) was diluted with PBS at a 1:200 ratio, and for the next 12.0 h, the diluted primary antibody solution was introduced into the medium channel and diffused into the ECM region of the biochip at 4.0 °C. Then, the ECM region was washed thoroughly with PBS to complete the target protein labelling. The secondary antibody, streptavidin-Alexa Fluor 555 (Bioss, China), was diluted with PBS at a 1:300 ratio and used to fill the biochip reservoirs. Then, the chip was kept at 37.0 °C in the dark for 12.0 h. Subsequently, the secondary antibody solution was removed, and the reservoirs were rinsed with PBS. For E-cad staining, the primary antibody, E-cadherin (24E10) rabbit mAb (Cell Signaling Technology, MA, USA), and the secondary antibody, streptavidin-Alexa Fluor 350 (Bioss, China), were used as described above.

## Results and discussion

### Characterization of composite ECM and its effect on oriented collagen fibers

Based on our prior discussion, a mixture of 3.0 mg mL<sup>-1</sup> collagen and 5.0 mg mL<sup>-1</sup> Matrigel was used to construct the composite ECM. Fig. 2A1–C1 show the SEM images (MIRA 3 FE-SEM, TESCAN, Czech) of collagen–Matrigel, collagen and Matrigel, respectively; the distinct porous microstructures of the three different systems can be clearly seen. Subsequent binarization processing and statistical analysis indicate that the pore sizes and density of the composite ECM are between those of pure collagen and Matrigel at the pre-set concentration (Fig. 2A2–C2 and D1 and D2). Hence, adjusting the mixing ratio of collagen and Matrigel allows us to control and generate composite ECM with different pore sizes and densities. The resulting composite ECM with properly selected mixing ratios not only can stabilize the diffusion of

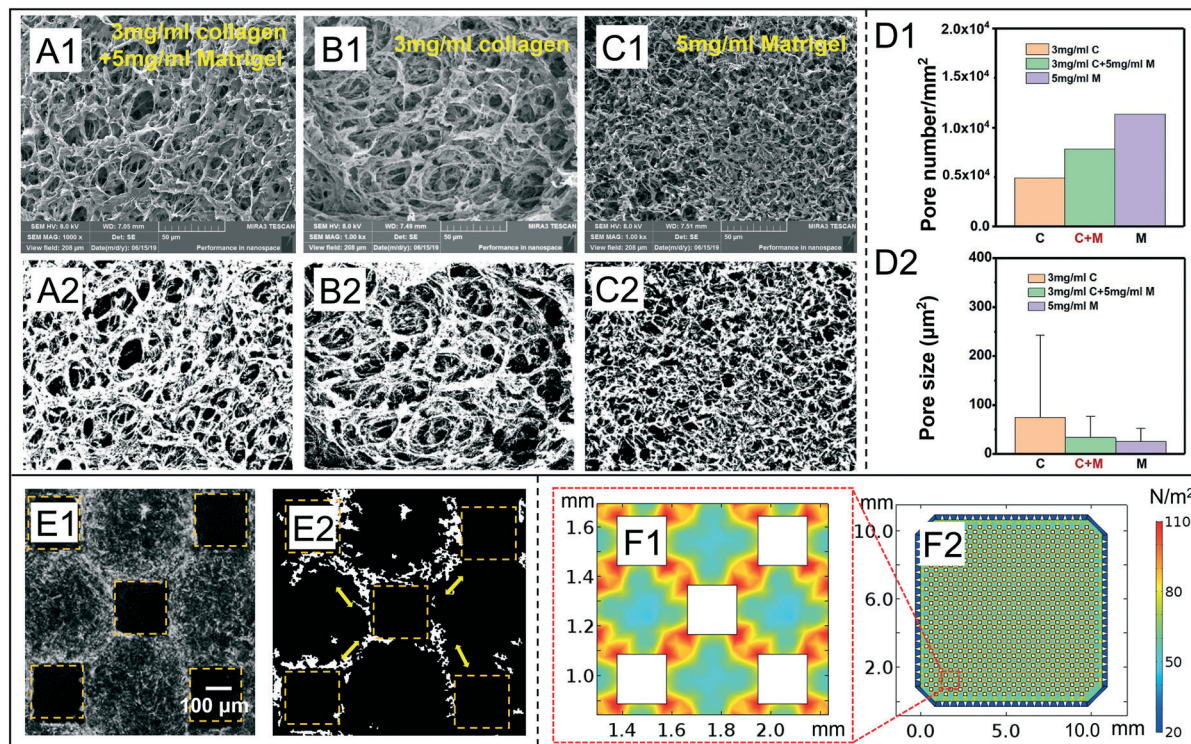


**Fig. 2** Characterisation of the collagen–Matrigel composite gel. (A1–C1) SEM images of the collagen–Matrigel composite, pure collagen, and pure Matrigel. (A2–C2) SEM images after binary processing. (D1 and D2) Pore number and size analysis of the gels. (E1 and E2) The relationship between collagen fibre distributions and square chambers. (F1) Stress field analysis of the ECM in the same regions as (E1) and (E2). (F2) Stress field of the entire ECM inside the chip.

small molecules of growth factors and drugs but also possesses superior material stability, allowing long-term time-lapse experiments up to 120.0 h.

It should be noted that similar to oriented collagen fibers observed in breast cancer tissues,<sup>8</sup> the aligned fiber structures induced by the square chamber can be easily produced in the composite collagen–Matrigel ECM. Fig. 2E1 shows a two-photon confocal microscope image (SP8, Leica, Germany) of the amplified chambers (yellow dashed line). White filament imaging is a second harmonic graphic (SHG) interpretation for collagen fibers and indicates their location and profiles. After binarization, the black and white images in Fig. 2E2 clearly indicate that linear collagen fibers (white) extend from the four square corners of a central chamber to the corners of its adjacent neighbors. Furthermore, COMSOL (Multiphysics 5.3a, Comsol, Sweden) simulations were performed to qualitatively analyze the stress distribution in the representative region of the biochip shown in Fig. 2E1 and E2 in order to better understand the origin of the observed fiber alignment. In particular, Fig. 2F1 shows the color map representing the distribution of the von Mises stress with blue to red representing the stress values from small to large. The detailed simulation method and parameters can be found in the ESI.† The simulation shows that in general, the stress in the corner zones (red) are twice that in the other regions, resulting from the well-known stress concentration effects. This is consistent with the

distribution of the aligned collagen fibers in Fig. 2E2, which implies that the fiber orientation is mainly induced by the stress concentration in the composite ECM. We note that similar effects were observed in our previous study, where Matrigel swelling stressed collagen and led to fiber orientation. Moreover, Fig. 2F2 shows the stress distribution in the entire ECM region. It can be seen that the stress distribution in the vicinity of individual chambers is almost identical. We therefore conclude that the high local stress orients the fibers (white) along the corner–corner directions as shown in Fig. 2E2, which in turn could enhance the invasion of MDA-MB-231-RFP cells significantly along these directions.

In addition, it is worth discussing the reason why a square chamber design is utilized instead of a circular design. Although circular chambers are supposed to be more appropriate to simulate *in vivo* cell niche structures due to the shape isotropy, it has been confirmed in our studies that the cell migration efficiency in the circular microchambers is extremely low and would prevent the device from examining the biochemical gradient effect on the migratory behavior of cancer cells, which is important for understanding cancer metastasis. In particular, both simulation and experiments indicate that the ECM outside circular chamber designs exhibit a uniform strain field, as illustrated in the ESI† (Fig. S1). In that case, the regions outside the chambers are mostly distributed with homogenous collagen fibers and metastatic

breast cancer cells MDA-MB-231 inside do not easily migrate into the ECM region across the boundary, which is consistent with our previous results,<sup>8</sup> and even though the cells do have slight migration, the efficiency is found to be extremely low. Hence, the square chamber design is finally utilized to introduce oriented fibers and enable cell migration with the desired efficiency.

### Establishment of the biochip model for multiple niches for tumor cells

In order to characterize the *in vitro* multiple niches for tumor cell microenvironment in our biochip system, two-photon confocal microscopy was employed. In Fig. 3A, the upper left image shows that the square chambers (black) are wrapped by the ECM with collagen fibers (white). The upper right image shows the 3D spatial configuration of a representative closed chamber with MCF-10A-GFP (green) and MDA-MB-231-RFP (red) cells cultured inside. The images below are the three-dimensional section views showing the cells inside the chamber. As these chambers are 200.0  $\mu\text{m}$  square and similar to the *in vivo* tumor cell niche scale (about 100–1750  $\mu\text{m}$ ),<sup>27</sup> they are ideal to mimic the *in vivo* structures *via* co-culture of metastatic MDA-MB-231-RFP cells and normal epithelial MCF-10A-GFP cells. The development of the *in vitro* tumor cell niche involves three stages (Fig. 3B). In stage I, MCF-10A-GFP cells (green) were uniformly implanted inside the chamber where they grow and attach to the inner walls. In stage II, after the MDA-MB-231-RFP cells (red) were introduced, the biochip was sealed by PDMS cover with pre-coated ECM. Then, the cells inside the chambers were co-cultured at 37.0  $^{\circ}\text{C}$  in a 5.0%  $\text{CO}_2$  environment. After 120.0 h, in stage III, the MDA-MB-231-RFP cells not only showed significant proliferation but also had broken down the niche

structures and migrated outside the chamber and into the ECM. More image data can be found in the ESI† (Fig. S2), indicating that the constructed niche structures are stable in space and time. We note that compared to *in vivo* complex structures, *e.g.*, ducts, our model has not realized uniform allocations of polarized epithelial cells, and the basement membrane has not been explicitly included either and their related functions, *e.g.*, the epithelial cells have not formed a polarized state, the cell-cell and cell-matrix interactions will be obstructed. The loss of basement membrane will influence the growth of epithelial cells and the invasion of tumor cells. However, the microfluidic chip has potential to be completed in the future to continue a more realistic approach to *in vivo* structures.<sup>28</sup>

### Establishment and dynamics of complex gradients

One advantage of our biochip is the four independent microfluidic channels at each side of the ECM region, which can help establish four different chemical gradients simultaneously. Compared to open chamber and channel space biochip designs,<sup>29,30</sup> our gradients are established and stabilized in a composite collagen–Matrigel gel and possess the advantages of superior controllability and reduced biochemical consumption. The constructed ECM not only provides cells with a physical microenvironment that better mimics the microenvironment *in vivo* but also induces much smoother and slower diffusive transport of small molecules of drugs and other chemicals due to its porous nature. The slow diffusion process through the porous ECM can significantly stabilize long-term quasi steady-state gradients in an easy-to-control manner. In particular, it just requires replacement of the medium in the reservoirs every 12.0 h and greatly benefits the simplicity of the system as well as ease of operations.

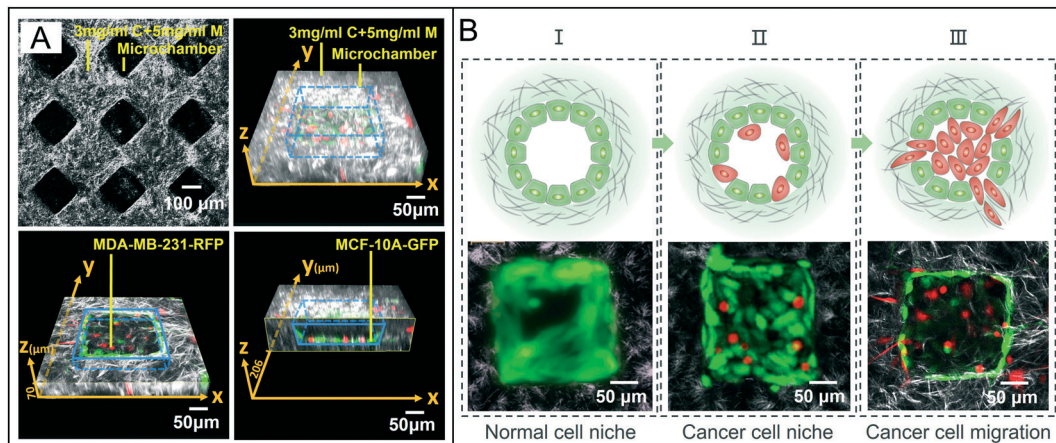


**Fig. 3** The characterisation and development of breast cancer niche *in vitro*. (A) Details of the microchambers and cells inside. The upper left inset shows the SHG of the microchambers consisting of collagen fibers (white). The upper right inset shows the spatial confocal image of a single chamber and the details of the chamber with fibers (white), MCF-10A-GFP cells (green) and MDA-MB-231-RFP cells (red) inside. The insets below are the three-dimensional section view along the x-y plane and x-z plane; the x-y plane is at 70  $\mu\text{m}$  along the z axis, the x-z plane is at 206  $\mu\text{m}$  along the y axis. The blue dotted and solid lines indicate the invisible and visible microchamber, respectively. (B) Development of mimicked breast cancer niche structures with cartoon illustrations and corresponding SHG images. The MCF-10A-GFP cells (green) represent mammary epithelial cells. The MDA-MB-231-RFP cells (red) represent metastatic breast cancer cells. The filaments represent ECM fibers. (I) Epithelial cells grew adherent to the chamber and formed normal cell niche. (II) After the cancer cells were introduced, the cancer cell niche was formed. (III) The cancer cells break down the cancer cell niche structures and migrate to the ECM.

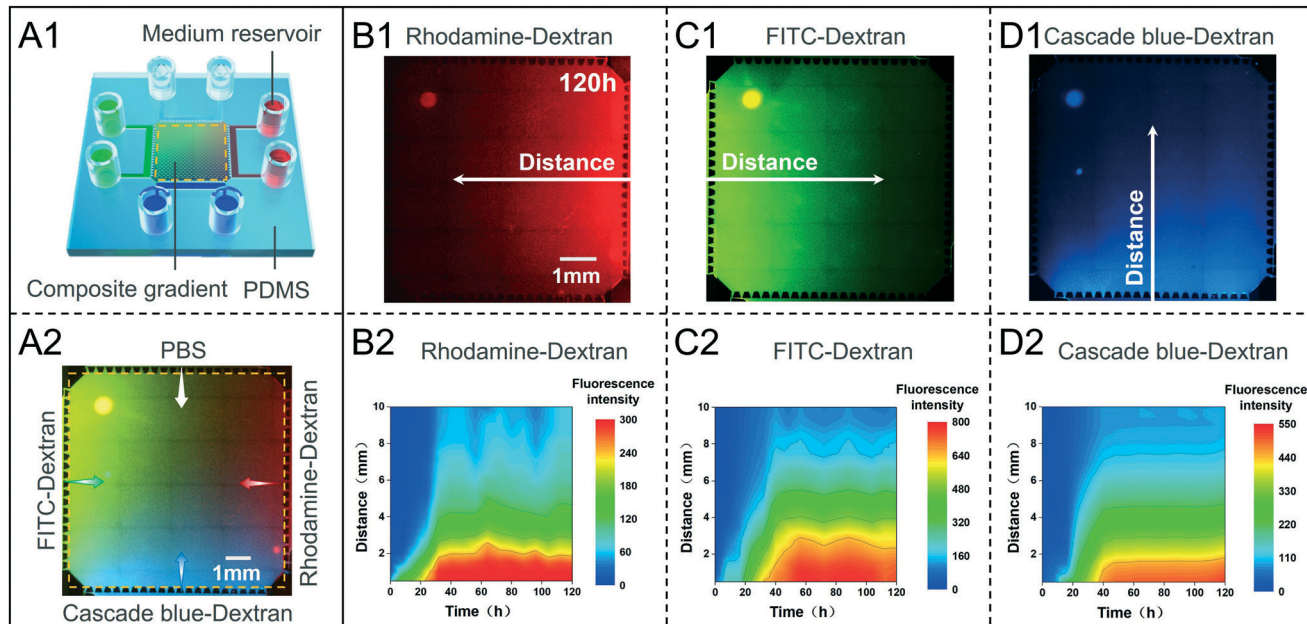


**Fig. 4** Dynamic establishment of the composite gradient. (A1) The introduction of rhodamine-dextran (red), FITC-dextran (green), Cascade blue-dextran (blue) and 1× PBS into the tetragonal microfluidic channels. (A2) A stable gradient is achieved after 120.0 h. (B1–D1) The fluorescent gradient in red, green and blue fluorescence. (B2–D2) Dynamic analysis of the individual gradients in space and time. x axis: time. y axis: distances from the microfluidic channels. Fluorescence intensity representing the specific concentration of the dyes.

As Fig. 4A1 shows, the biochip external medium reservoirs are filled with different media and can establish composite gradients in the biochip ECM region (orange) *via* diffusion. For testing, the upper, left, right and lower reservoirs were injected with PBS, fluorescent dyes FITC-dextran ( $3.0 \times 10^3$  Da, green), rhodamine-dextran ( $1.0 \times 10^4$  Da, red), and Cascade Blue-dextran ( $3.0 \times 10^3$  Da, blue). These dyes are broadly used for gradient experiments and tests.<sup>31,32</sup> During the experiment, the dyes were refreshed every 12.0 h and the biochip was imaged every 8.0 h for 120.0 h until all the gradients reached the corresponding stable states, as shown in Fig. 4B1–D1. Fig. 4A2 shows that after the dyes flow into the tetragonal channels, they diffuse towards the center region and gradually establish an independent chemical gradient. The plots in Fig. 4B2–D2 show the diffusion dynamics in time and space across the biochip, where each gradient establishes gradually over time. However, it is difficult to precisely determine the stabilization time for the dye gradients. For accuracy, each dye experiment has been repeated three times and the details can be found in the ESI.† As shown in Fig. S3,† all the dye systems appear to reach the steady state between 40 and 60 hours, as can be clearly seen from the temporal evolution of the averaged concentration field which reaches a plateau after this transition time. Since the transition to steady state is rather smooth than sharp, it is still difficult to determine a precise time point for the transition. Otherwise, since all of the dyes have good water solubility, their distribution in solution would be in molecular form. The molecular weights of the three dyes are  $1.0 \times 10^4$  Da (rhodamine-dextran),  $3.0 \times 10^3$  Da (FITC-dextran) and  $3.0 \times 10^3$  Da (Cascade blue-dextran). According to the SEM image in Fig. 2A1, the collagen–Matrigel composite ECM is a porous

structure and the average pore size is about 3.0  $\mu\text{m}$ , which is much larger than the molecules of dyes and drugs. In this case, their diffusion dynamics has been shown to be mainly governed by the porous microstructure (*e.g.*, *via* various fiber–molecule interactions such as collision and uptake) and is less sensitive to their molecular weights. Therefore, the diffusion dynamics of these dyes obeys the homogenized diffusion equations, with an effectivity diffusivity  $D$ .<sup>33</sup> The details can be found in the ESI.†

As a comparison, a new control experiment uses rhodamine-dextran at the same concentration, placed in an identical chip configuration but without gel-based ECM (see details in the ESI.†). It can be seen that once the rhodamine-dextran is released at the side channel, the diffusion occurs very rapidly, and the environment is homogenously colored with the dye after 1.0 h (Fig. S4(B1 and B2†)). Hence, we can draw a conclusion that the composite ECM plays a crucial role in long-term stabilization of biochemical gradients. Moreover, previous studies demonstrated that EGF and other growth factors are able to diffuse in gels such as collagen to influence cell dynamics.<sup>34</sup> Based on this peculiarity, our MACECM device can establish a complex gradient to mimic the drug diffusion *in vivo*, which provides a platform for high-throughput testing of drug effects on cells.

#### Spatial–temporal dynamics of cell growth and migration in complex gradients

Another unique feature of our high-throughput biochip is that it contains 642 micro chambers which are embedded in the ECM; by systematically controlling the stable spatial–temporal gradients across the entire chip, each micro

chamber is supposed to experience different local concentrations of the biochemicals, which could potentially induce distinct cell behaviors and physiology. Compared to other high-throughput biochip platforms for drug testing, our system focuses on establishing individual micro-environments with distinct combination of biochemicals (e.g., growth factors and drugs) in the ECM, which allows one to systematically investigate the cells' unique responses to these factors and perform rigorous statistical analysis.

In particular, after MDA-MB-231-RFP cells and MCF-10A-GFP cells were injected into the biochip chambers according to the previous procedure, we observed cell migrations influenced by the established chemical gradients. Here, a combination of stable 1× EGF ( $0.04 \mu\text{g mL}^{-1}$ ), 2× EGF ( $0.08 \mu\text{g mL}^{-1}$ ), batimastat ( $66.0 \mu\text{g mL}^{-1}$ ) and 7rh ( $22.44 \mu\text{g mL}^{-1}$ ) gradients in the ECM chambers were established as shown in Fig. 5A. During the experiment, the medium was refreshed every 12.0 h, maintaining a consistent reservoir level of medium; fluorescence images of cells were taken every 24.0 h and up until 120.0 h.

The reason that these three chemicals are selected is as follows: EGF is a widely used promoting factor. It not only can promote the growth of MCF-10A-GFP cells<sup>35,36</sup> but also facilitate the proliferation, migration and invasion of MDA-MB-231-RFP cells.<sup>37,38</sup> Batimastat is a potent inhibitor of matrix metalloproteinases (MMPs). It may help maintain the expression of E-cad protein and the structural integrity of epithelial cells<sup>39,40</sup> and further inhibit migrations of MDA-MB-231-RFP cells. Moreover, 7rh as an inhibitor of discoidin domain receptor 1 (DDR1) could down-regulate the expression of DDR1 and reduce the specific binding with collagen to effectively inhibit the proliferation and migration of cancer cells.<sup>41,42</sup> Furthermore, with the introduction of batimastat and 7rh, we are able to test our hypothesis. The two drugs are considered to have significant inhibitory effects on cancer cell invasion but have not yet been applied clinically.<sup>40,42</sup> Hence, our hypothesis is that the MACECM is able to verify the effects of these drugs on metastatic cancer cells and normal epithelial cells. That is, with co-culture of MDA-MB-231-RFP cells and MCF-10A-GFP cells under 7rh

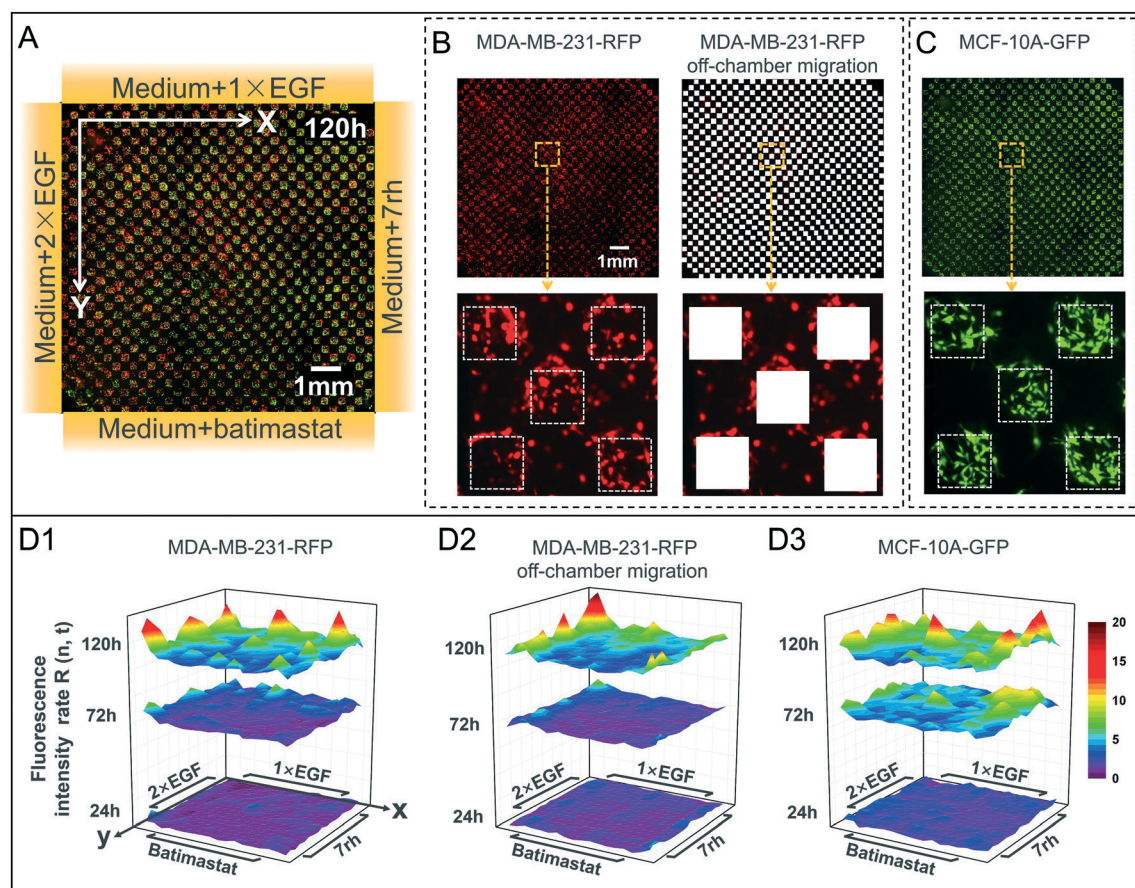


**Fig. 5** Cell dynamic development and analysis in microchamber arrays. (A) Cell distribution at 120.0 h in composite biochemical gradients. Red and green indicate the MDA-MB-231-RFP and MCF-10A-GFP cell distributions, respectively. The four microchannels (orange) are introduced with EGF ( $0.08 \mu\text{g mL}^{-1}$  and  $0.04 \mu\text{g mL}^{-1}$ ), batimastat ( $66.0 \mu\text{g mL}^{-1}$ ) and 7rh ( $22.44 \mu\text{g mL}^{-1}$ ). (B) The fluorescence images of MDA-MB-231-RFP cell overall development and their off-chamber migration in the ECM region, with their respective amplified images in the localised regions. (C) The fluorescent images of MCF-10A-GFP cell overall development and their amplified images in the localised region. (D1–D3) The fluorescence intensity rate change of MDA-MB-231-RFP cells, MDA-MB-231-RFP cells off-chamber migration and MCF-10A-GFP cells in time and ECM regional space. The data selected were 24.0, 72.0 and 120.0 h. The colour bar represents rate increase (from purple to red).

and batimastat compound drugs, our result is expected to demonstrate MDA-MB-231-RFP cells are much more sensitive to the drug gradients, while the growth and proliferation of MCF-10A-GFP cells are not significantly affected. Moreover, through analyzing the biophysical behaviors of various cells under the influence of dynamic and complex drug gradients with continuous optic imaging, we expect to verify that the chip designed in this study may provide a useful approach for high-throughput testing and screening of drugs and individualized cancer treatment.

Fig. 5B and C show the images of MDA-MB-231-RFP cells (red) and MCF-10A-GFP cells (green) at 120.0 h. MDA-MB-231-RFP cells can grow in the cavity of the chamber and they may also migrate outside the chamber (Fig. 5B, left inset). Here, the cells outside the chamber were further isolated and designated as migratory cells (Fig. 5B, right inset). Specifically, the region inside the microchamber cavity (white dashed line) was temporarily removed for additional analysis of cell dynamics. In the enlarged view in Fig. 5B, the MDA-MB-231-RFP cells in the selected region clearly migrated outside the chambers into the ECM region. On the other hand, most of the MCF-10A-GFP cells in this region uniformly adhered to the inner wall of the chambers at 0 h (Fig. 3B). However, at 120.0 h, the cells were dispersed, and several cells had migrated outside the microchamber, as shown in the lower inset (Fig. 5C). It can be considered that the off-chamber migration of MCF-10A-GFP cells may be affected by the growth and migration of MDA-MB-231-RFP cells.

Furthermore, for quantitative analysis of the spatial-temporal dynamics of proliferation, migration and growth of MDA-MB-231-RFP cells and MCF-10A-GFP cells under the complex concentration gradients, the biochip images were captured every 24.0 h under consistent imaging conditions and the complete time-lapse data can be found in the ESI† (Fig. S5). According to previous studies, the fluorescence intensity has been shown to be a reasonable parameter for cell number indication, *i.e.*, the cell number is proportional to cell fluorescence intensity,<sup>43,44</sup> so we isolated the image using the approaches described above and plotted the dynamic fluorescence intensity changes of MDA-MB-231-RFP and MCF-10A-GFP at different time points as an indirect assessment of the cell number variations (Fig. 5D). In detail, the ECM regions were divided into 144 sub-regions of equal size and the fluorescence intensity was analysed using MATLAB. The fluorescence intensity of the cells in a specific region  $n$  at time  $t$  is represented by  $I(n, t)$ , where  $n = 0, 1, \dots, 144$  and  $t = 0, 24, \dots, 120$ . Therefore, in order to demonstrate the comprehensive dynamics of cell behaviors, including growth, proliferation and migration in each sub-region at different time points, the cell fluorescence intensity rate  $R(n, t)$  is employed and defined as

$$R(n, t) = I(n, t)/I(n, 0) \quad (1)$$

where  $I(n, 0)$  is the initial 0 h cell fluorescence intensity of the grid  $n$  in the ECM and  $I(n, t)$  is the  $t$  hour cell fluorescence intensity of the same grid  $n$  in the ECM.

In Fig. 5D1, the fluorescence intensity change of MDA-MB-231-RFP cells at 24.0 h is not obvious in comparison with the 0 h intensity map. After 72.0 h of incubation, the fluorescence intensity of the cells in the left ( $2\times$  EGF) region increased significantly, and several regions reached about 5-fold increase compared to that at 0 h. After 120.0 h, the rate of change in fluorescence intensity at the left ( $2\times$  EGF) and the upper ( $1\times$  EGF) continued to increase, especially at the junction of  $2\times$  EGF and  $1\times$  EGF, where the fluorescence intensity of the cells increased to 15–20-fold that at 0 h. Fig. 5D2 shows the fluorescence intensity of cells migrating into the ECM at the same time, which is also unobvious at 24.0 h. The fluorescence intensity of sporadic regions near  $2\times$  EGF and  $1\times$  EGF at 72.0 h was about 5-fold that of 0 h and reached 15–20-fold that of 0 h at 120.0 h. These results indicate that the chemical gradient combination of EGF, 7rh and batimastat can significantly influence the proliferation and migration of MDA-MB-231-RFP cells. Fig. 5D3 shows that the change in fluorescence intensity of MCF-10A-GFP at 24.0 h was also low; however, at 72.0 h, this had increased significantly. In many sub-regions, the fluorescence intensity was approximately 5-fold that of 0 h, and in a few sub-regions, it even reached about 10-fold increase. The fluorescence intensity of the cells continued to increase at 120.0 h and in most areas was approximately 10-fold that at 0 h, with some sub-regions reaching a 15–20-fold increase. Notably, MCF-10A-GFP cells have more uniform distributions in chemical gradients, which appeared to be independent of the detailed effect from the chemicals.

In order to demonstrate more comprehensively the capabilities and advantages of the platform, it is necessary to explore cell behaviors under growth factor/drug-free and independent growth factor/drug conditions, following the identical experimental setup as shown above. Fig. 6A(I–VI) show the fluorescence intensity and distribution of MDA-MB-231-RFP and MCF-10A-GFP cells at 120 h under conventional medium (growth factor/drug-free), single  $2\times$  EGF,  $1\times$  EGF, batimastat, 7rh and composite chemical gradients. Furthermore, the images have been processed following the same protocol shown in Fig. 5B–D and present the quantification of the cell fluorescence intensity rate in space, *i.e.*, the growth and migration of MDA-MB-231-RFP cells as well as the growth of MCF-10A-GFP cells. The results are shown in Fig. 6B1–B3.

First, regarding the growth factor/drug-free experiment, *i.e.*, the four side channels were with the same culture medium, MDA-MB-231-RFP cells, off-chamber MDA-MB-231-RFP cells and MCF-10A-GFP cells have fairly uniform distributions across the chamber space. In independent addition of  $2\times$  EGF and  $1\times$  EGF scenarios, the average fluorescence intensity rates of MDA-MB-231-RFP cells and off-chamber MDA-MB-231-RFP cells are higher than that of the growth factor/drug-free group, and the intensity with  $2\times$  EGF is higher than  $1\times$  EGF, particularly near the side of the EGF channels. These results not only confirm the EGF's promoting effects on cell growth and migration again,<sup>35,37</sup>

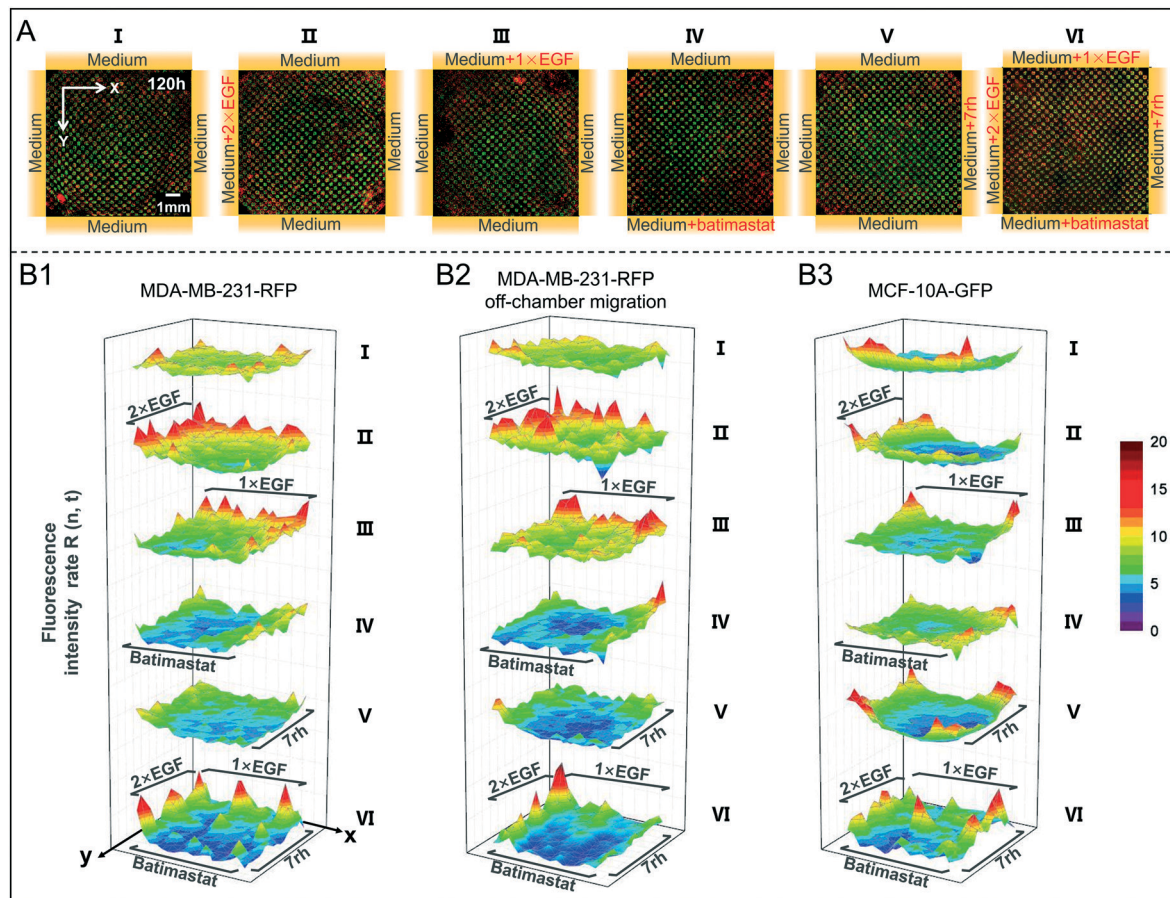


**Fig. 6** The systematic analysis of cells in microchamber arrays under various environments. (A) Images of cell spatial distributions at 120.0 h in conventional medium (control) (I), single-added chemicals and composite chemicals (VI), from left to right. Single-added chemical experiments are introduced with 2×EGF ( $0.08 \mu\text{g ml}^{-1}$ ) (II), 1×EGF ( $0.04 \mu\text{g ml}^{-1}$ ) (III), batimastat ( $66.00 \mu\text{g ml}^{-1}$ ) (IV) and 7rh ( $22.44 \mu\text{g ml}^{-1}$ ) (V) on one channel of the chip. Red and green indicate the MDA-MB-231-RFP and MCF-10A-GFP cell distributions, respectively. (B1–B3) The fluorescence intensity rate of MDA-MB-231-RFP cells, MDA-MB-231-RFP cells off-chamber migration and MCF-10A-GFP cells in the control experiment, single-added chemicals and composite chemical experiments, from top to bottom. The color bar indicates the cell fluorescence rate increase (from purple to red).

but also demonstrate the effect of chemical gradients. In contrast, compared to the growth factor/drug-free group, the average fluorescence intensity rates of MCF-10A-GFP cells present no apparent increase or decline. This is because while EGF promotes the growth of MCF-10A-GFP cells, it has more significant effects on the growth and migration of MDA-MB-231-RFP cells, which in turn inhibit the aggregation and proliferation of MCF-10A-GFP cells<sup>45</sup> due to limited sources. Regarding the independent addition of batimastat and 7rh drugs, compared to growth factor/drug-free groups, the average fluorescence intensity rates of MDA-MB-231-RFP cells and off-chamber MDA-MB-231-RFP cells are lowered, particularly for off-chamber MDA-MB-231-RFP cells. This indicates that batimastat and 7rh have strong inhibition effects on the MDA-MB-231-RFP cell growth and migration,<sup>39,41</sup> and the cell fluorescence intensity near the drug side is significantly lower than that of other regions, which again has demonstrated the gradient effect. Meanwhile, the average fluorescence intensity rates of MCF-10A-GFP cells have just a slight decline and indicate batimastat or 7rh's weak effect on MCF-10A-GFP cells.

Finally, in the composite growth factor/drug case, the average fluorescence intensity rates of MDA-MB-231-RFP cells and off-chamber MDA-MB-231-RFP cells present similar trends to the single addition of growth factor/drug cases, *i.e.*, the fluorescence intensity is stronger near the EGF channels and is weaker near the batimastat or 7rh channels. However, if probing into detailed cell fluorescence intensity, the case of composite chemicals has slight differences compared to single addition cases. This may be due to the cells having different responses to simultaneously applied four chemicals. The detailed studies of differences between individual addition of chemicals and composite chemicals need more quantitative experiments and analysis in the future.

In short, through the performance of comparable and parallel studies of single chemical and composite chemical gradient effects, the new results demonstrate again that our chip platform with 642 microchambers is ideal for high-throughput and quantitative analysis of cell response to different drugs and growth factors. In addition, the chip platform not only supports studies of cell response to

composite chemical gradients but also is feasible to investigate the effects of single chemical gradients. The results are reasonable and consistent and again demonstrate the uniqueness of this platform compared to other 2D and 3D drug screening systems.

### Regional analysis of cell dynamics

For direct comparison of the joint effects of adjacent chemical gradients on the growth and migration of the two different types of cells, we divided the ECM region into four quadrant regions:  $Q_I$ ,  $Q_{II}$ ,  $Q_{III}$  and  $Q_{IV}$  (Fig. 7A, left diagram). We then analysed the variation in fluorescence intensity of the designated cell population at 120.0 h in each region separately with MDA-MB-231-RFP cells coded as blue, MDA-MB-231-RFP cells migrating into the ECM are coded as red and MCF-10A-GFP cells are coded as green. After being designated in this way, each region has two main types of gradients, which represents the combination of batimastat-7rh, 7rh-1×EGF, 1×EGF-2×EGF and 2×EGF-batimastat. It can be seen that the variation rate of fluorescence intensity of MDA-MB-231-RFP cells and MDA-MB-231-RFP cells migrating into the ECM region gradually increased from  $Q_I$  to  $Q_{IV}$ , whereas the rates in  $Q_{II}$  and  $Q_{III}$  were comparable. This indicates that the combined influence of increased batimastat and 7rh, along with the decreased concentration of EGF, has a strong inhibitory effect on the growth and migration of MDA-MB-231-RFP cells ( $Q_I$ ). However, when EGF was enhanced and the concentration of batimastat and 7rh was decreased, EGF strongly stimulated the

MDA-MB-231-RFP cell growth and migration ( $Q_{IV}$ ). Intriguingly, the difference in the variations of fluorescence intensity in MCF-10A-GFP in the four regions was not particularly obvious. In  $Q_{III}$  and  $Q_{IV}$  (with the 2×EGF action), the variation rate of fluorescence intensity of MCF-10A-GFP cells slightly decreased. This implies that the growth and proliferation of MCF-10A-GFP may be additionally affected by the growth and interaction of MDA-MB-231-RFP cells in addition to EGF stimulation.<sup>45</sup>

The adjacent boundaries of the four regions represent the areas with the strongest combination of chemical concentrations and the most significant effect for a particular combination, and therefore, the four corners of the square area ( $S_1-S_4$ ) were selected for further analysis (Fig. 7A, right diagram). The changes in the fluorescence intensity of the two types of cells are essentially consistent with the left diagram in Fig. 7A, indicating that the changes in the fluorescence intensity of the cells in the  $Q_I-Q_{IV}$  region are mainly determined by the cells in the  $S_1-S_4$  region near the reagent pipelines. However, simultaneously, the variations of the fluorescence intensity for migrating MDA-MB-231-RFP cells in  $S_2$  and  $S_3$  were different, *i.e.*, the latter was higher than the former, which indicates that the combined effect (combinatorial effects) of 2×EGF with batimastat compound treatment in MDA-MB-231-RFP cells resulted in a mildly elevated migration rate than that of the combined effect of 1×EGF with 7rh. This result further demonstrates that the promotional effect of higher concentrations of EGF surpass the inhibitory effect of batimastat on the migration of MDA-MB-231-RFP cells in the MACECM.

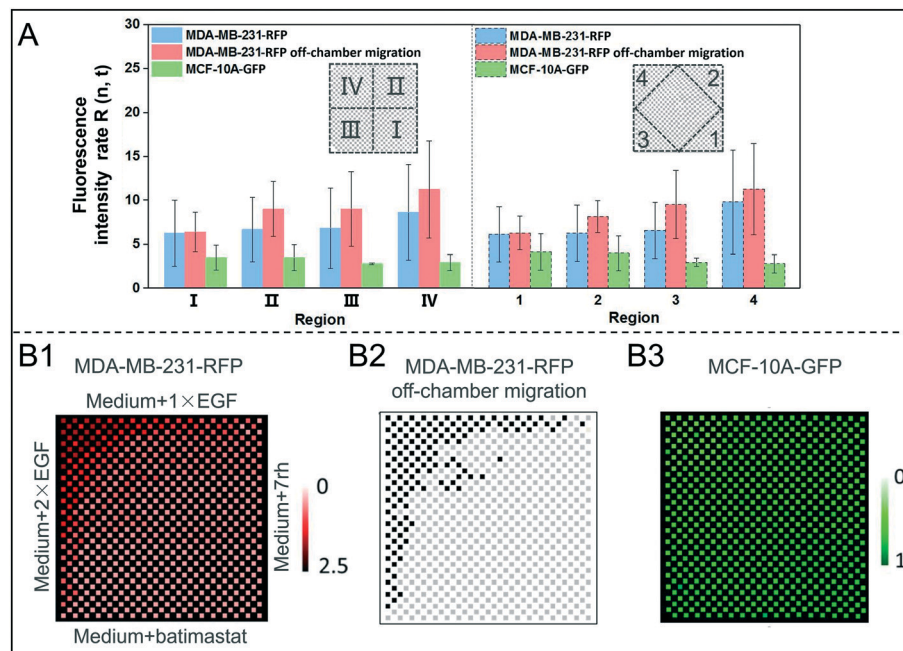


**Fig. 7** Regional analysis of cell dynamics. (A) Regional analysis of biochemical gradient influence on MDA-MB-231-RFP and MCF-10A-GFP cell development. The gradients have more influences on MDA-MB-231-RFP cell proliferation and migration, while they have less effect on MCF-10A-GFP cells. In addition, the data could clearly clarify the effects in the regions with different combinations of the biochemicals. (B1–B3) Simulation results of cell development and migration in ECM regions applied with the composite gradient, which elaborates the above experimental results.

## Computational model for the spatiotemporal evolution of the cell population in the micro-biochip

To complement our experimental studies, we also developed a computational model for the spatiotemporal evolution of the cell populations in the biochip. Our model is based on continuous diffusion equations for inhibitors and growth factors that are coupled with equations governing cell population dynamics. The details of our computational model and methods are provided in the ESI.<sup>†</sup>

The population distribution for MDA-MB-231-RFP cells and MCF-10A-GFP cells are shown in Fig. 7B1 and B3, respectively, where darker colour indicates greater local cell densities. It can be clearly seen that the MDA-MB-231-RFP cells are highly proliferative in the regions with high EGF and low inhibitor concentrations, that is, the upper left corner of the biochip. On the other hand, the distribution of MCF-10A-GFP cells was more spatially uniform and exhibited less cell population in the regions with more MDA-MB-231-RFP cells. This is due to competition between space and EGF between the two cell types. These results are consistent with the experimental observations and further demonstrate the

effectiveness of the high-throughput biochip. We also introduced a migration metric to quantify migration of the MDA-MB-231-RFP cells, that is, corresponding to the MDA-MB-231-RFP off-chamber migration in the experiments (Fig. 7B2). It is noted that for non-migrate cells, the maximal value for the local cell density is unity, corresponding to the case where the entire microchamber is occupied by the cells. In the simulations, the density of MCF-10A-GFP cells,  $\rho_\beta$ , is always smaller than one, that is,  $\rho_\beta < 1$ . However, for MDA-MB-231-RFP cells, owing to their strong migration ability, the cell density,  $\rho_\alpha$ , can be greater than one,  $\rho_\alpha > 1$ , indicating that the cells break the constraint of the micro-chamber and migrate to the surrounding ECM. Therefore, the migration metric is defined as the density at location  $x$  in access to unity, that is:

$$M_1(\mathbf{x}, t) = \min \{ \rho_\alpha(\mathbf{x}, t) - 1, 0 \} \quad (2)$$

Microchambers containing MDA-MB-231-RFP cells have significant migration (*i.e.* those with  $M_1 > 0$ ) (Fig. 7B2) and follow a distribution pattern similar to that of the MDA-MB-231-RFP cell population.

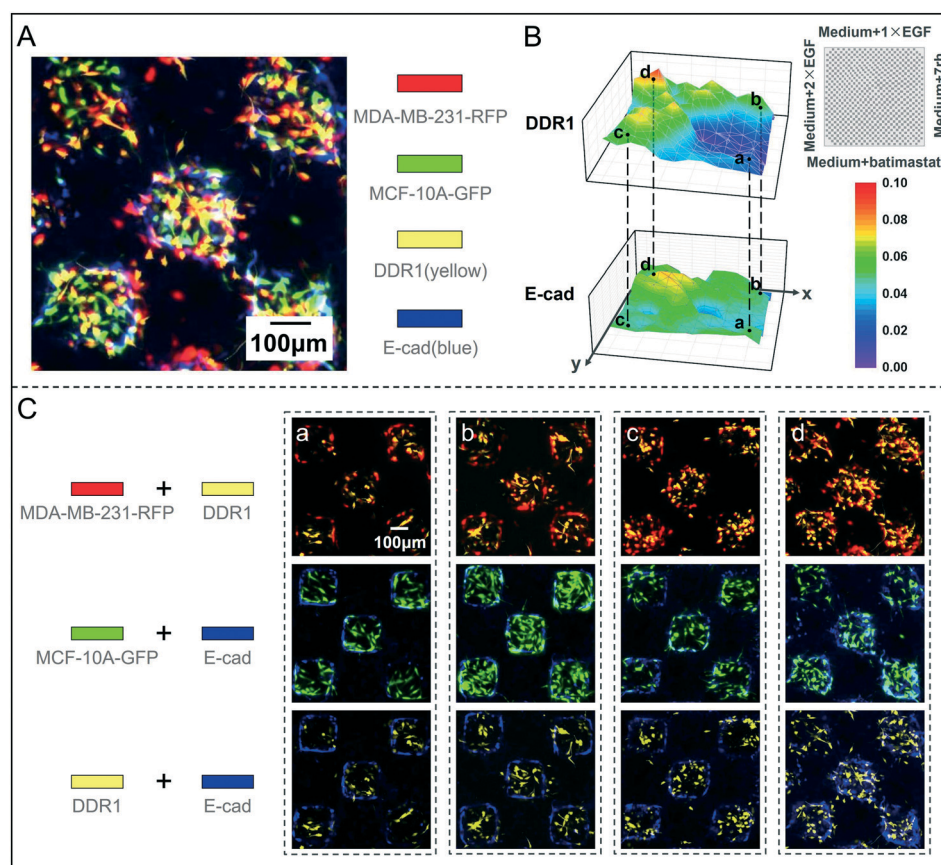


Fig. 8 Immunofluorescence analysis of cell proteins. (A) The fluorescence composite image of MDA-MB-231-RFP cells (red), MCF-10A-GFP cells (green), DDR1 (yellow) and E-cad (blue) at 120.0 h. (B) Distribution of DDR1 (top) and E-cad (bottom) in the entire ECM region. Scale bar represents fluorescence intensity increase (from purple to red). (C) The composite fluorescence pictures of cells and proteins at specific locations (a-d) in the ECM region.

## Differential effect of complex biochemicals on E-cad and DDR1 expression in MCF-10A-GFP and MDA-MB-231-RFP cells

Immunofluorescence labelling of candidate protein markers is one of the most widely used quantitative methods for the simultaneous assessment of multiple proteins in the same cell or among different cell types.<sup>46</sup> Through the fluorescence imaging of cell-specific proteins, we were able to evaluate biological and phenotypic changes, such as cell growth and migration, in complex gradients of chemical compounds and specific microenvironments as stated above. Here, we selected DDR1 as a biomarker for metastatic breast cancer cells and E-cad as a marker for epithelial cells, labelled with yellow fluorescence dye and blue fluorescence dye, respectively. As discussed above, both MDA-MB-231-RFP cells and MCF-10A-GFP cells were transfected with red and green fluorescence, respectively. Therefore, under the confocal microscope, we were able to obtain the overlay fluorescence image of DDR1 (yellow) and E-cad (blue) in both MDA-MB-231-RFP (red) and MCF-10A-GFP (green) cells in each microchamber region and adjacent matrix region of the biochip (Fig. 8A). As expected, E-cad was only detected in MCF-10A-GFP cells but not in MDA-MB-231-RFP cells. In contrast, DDR1 is universally expressed in MDA-MB-231-RFP but is rarely expressed or undetectable in epithelial MCF-10A-GFP cells, which is also consistent with previous studies.<sup>47,48</sup>

According to the same processing method as depicted in Fig. 5B and C, the average fluorescence intensity and distribution of DDR1 protein (top) and E-cad protein (bottom) in the ECM region were quantitatively measured (Fig. 8B). It can be seen that the expression of DDR1 is highest in the regions near the 1× EGF and 2× EGF pipelines (the fluorescence intensity is approximately 0.09), whereas it is very low near the 7rh and batimastat pipelines (fluorescence intensity of approximately 0.02). In contrast, the distribution of E-cad expression was even among all the ECM regions (the fluorescence intensity is 0.04–0.06). Moreover, we further analysed the immunofluorescence images of the four representative points (a–d) shown in Fig. 7A and re-evaluated the association of cell growth and migration behaviors with the expression levels of DDR1 and E-cad proteins (Fig. 8C). For MDA-MB-231-RFP cells, the DDR1 protein expression and cell migration at point (d) is significantly higher than that at point (a). However, for MCF-10A-GFP cells, the E-cad protein expression and cell density at point (d), with the highest EGF concentration, did not significantly increase in comparison with the other selected points. Hence, it can be considered that DDR1 protein is important for regulating the migration of MDA-MB-231-RFP cells. The proliferation, migration and DDR1 protein expression of MDA-MB-231-RFP cells were remarkably enhanced by EGF but inhibited by the exposure to 7rh and batimastat. Meanwhile, the expression level of E-cad protein was not significantly affected after exposure to the combination gradients of these three compounds. In short, the combined effect on the growth and migration of MCF-

10A-GFP cells was not as significant as that observed in MDA-MB-231-RFP cells.

## Conclusion

Our MACECM system, with a quadrangular gradient biochip and resolution microscopy imaging, has shown versatile and multi-task capabilities for the analysis of cell behavior and underlying molecular mechanisms in complex biochemical environments and in a spatiotemporal manner. It can simultaneously study multiple cell samples in high throughput and at single-cell scale. This biochip system can also distinguish the complex behavior of a single cell of a specific type or mixed multicellular system under co-culture conditions and statistically quantify the differentially expressed proteins of interest. In particular, the chip may be able to act as a new drug screening platform that is able to facilitate quantitative verification of drug effects on different cells in a single experiment.

The experimental platform can be reformatted and applied to a wide range of cellular behavior and biological studies of cancer cells and healthy cells by changing the internal details logically. There is potential for further development of this biochip to maximize both its research and application potentials. For instance, the basement membrane needs to be considered for constructing *in vitro* lumen structures with ECM and the device will facilitate cell invasion studies. In addition, we also plan to seed patient-derived tumor cells in the biochip to explore the pathophysiological behavior of tumor cells and their responsiveness to a panel of therapeutic drugs or various combinations of the drugs. Thus, the future development of the MACECM system may provide us with a new platform for the screening and evaluation of effective candidate drugs for a particular patient in the era of personalized cancer therapy.

## Author contributions

J. Y. and L. L. designed the research; J. Y., G. L., Y. J., Y. L., G. W., H. Z., Q. F., F. Y., X. Z., G. C., K. S. and L. L. performed the research; J. Y., G. L., Y. J., Y. Z., L. Z., J. S., K. S., Y. L., S. L. and L. L. analysed data; J. Y., G. L., Y. J., K. S., Y. L. and L. L. wrote the paper.

## Conflicts of interest

There are no conflicts to declare.

## Acknowledgements

We gratefully acknowledge support by the National Natural Science Foundation of China (11974066, 11674043, 81172066, 81472858, 11704404) and a major research project award from the NSFC (915291003), the Fundamental and Advanced Research Program of Chongqing (cstc2019jcyj-msxmX0477), the Fundamental Research Funds for the Central Universities (2019CDYGYB007) and the Capital Health Development

Research Project (Grant No. 2020-2-2072), A Start-up Fund (08-1286-001) and the Fund for “Innovative Team on Cancer Metabolism” (2209-16) from the 2nd Affiliated Hospital, Chongqing Medical University, Chongqing, P.R. China. In addition, we would like to thank Miss Qin Deng at the Analytical and Testing Center of Chongqing University for her assistance with immunofluorescence imaging and analysis. Y. J. thanks the Arizona State University for support and Peking University for hospitality during his sabbatical leave.

## References

- 1 L. A. Torre, F. Bray, R. L. Siegel, J. Ferlay, J. Lortet-Tieulent and A. Jemal, *Ca-Cancer J. Clin.*, 2015, **65**, 87–108.
- 2 U. Veronesi, P. Boyle, A. Goldhirsch, R. Orecchia and G. Viale, *Lancet*, 2005, **365**, 1727–1741.
- 3 J. Li, *Keji Daobao*, 2014, **32**, 22–26.
- 4 A. J. Redig and S. S. McAllister, *J. Intern. Med.*, 2013, **274**, 113–126.
- 5 P. S. Steeg and D. Theodorescu, *Nat. Clin. Pract. Oncol.*, 2008, **5**, 206–219.
- 6 S. Alexander, B. Weigelin, F. Winkler and P. Friedl, *Curr. Opin. Cell Biol.*, 2013, **25**, 659–671.
- 7 A. Malandrino, M. Mak, R. D. Kamm and E. Moeendarbary, *Extreme Mech. Lett.*, 2018, **21**, 25–34.
- 8 W. Han, S. Chen, W. Yuan, Q. Fan, J. Tian, X. Wang, L. Chen, X. Zhang, W. Wei, R. Liu, J. Qu, Y. Jiao, R. H. Austin and L. Liu, *Proc. Natl. Acad. Sci. U. S. A.*, 2016, **113**, 11208–11213.
- 9 K. M. Riching, B. L. Cox, M. R. Salick, C. Pehlke, A. S. Riching, S. M. Ponik, B. R. Bass, W. C. Crone, Y. Jiang, A. M. Weaver, K. W. Eliceiri and P. J. Keely, *Biophys. J.*, 2014, **107**, 2546–2558.
- 10 X. Yang, K. Li, X. Zhang, C. Liu, B. Guo, W. Wen and X. Gao, *Lab Chip*, 2018, **18**, 486–495.
- 11 S. J. Hachey and C. C. W. Hughes, *Lab Chip*, 2018, **18**, 2893–2912.
- 12 Y. Choi, E. Hyun, J. Seo, C. Blundell, H. C. Kim, E. Lee, S. Lee, A. Moon, W. K. Moon and D. Huh, *Lab Chip*, 2015, **15**, 3350–3357.
- 13 J. Avesar, Y. Blinder, H. Aktin, A. Szklanny, D. Rosenfeld, Y. Savir, M. Bercovici and S. Levenberg, *Anal. Chem.*, 2018, **90**, 7480–7488.
- 14 N. L. Jeon, S. K. W. Dertinger, D. T. Chiu, I. S. Choi, A. D. Stroock and G. M. Whitesides, *Langmuir*, 2000, **16**, 8311–8316.
- 15 V. Vickerman, J. Blundo, S. Chung and R. Kamm, *Lab Chip*, 2008, **8**, 1468–1477.
- 16 Y. Shin, S. Han, J. S. Jeon, K. Yamamoto, I. K. Zervantonakis, R. Sudo, R. D. Kamm and S. Chung, *Nat. Protoc.*, 2012, **7**, 1247–1259.
- 17 D. R. Stamov and T. Pompe, *Soft Matter*, 2012, **8**, 10200–10212.
- 18 C. Liverani, L. Mercatali, L. Cristofolini, E. Giordano, S. Minardi, G. D. Porta, A. D. Vita, G. Miserocchi, C. Spadazzi, E. Tasciotti, D. Amadori and T. Ibrahim, *Cell. Mol. Bioeng.*, 2017, **10**, 223–234.
- 19 N. Gjorevski and C. M. Nelson, *Integr. Biol.*, 2010, **2**, 424–434.
- 20 C. A. Grant, D. J. Brockwell, S. E. Radford and N. H. Thomson, *Biophys. J.*, 2009, **97**, 2985–2992.
- 21 C. S. Hughes, L. M. Postovit and G. A. Lajoie, *Proteomics*, 2010, **10**, 1886–1890.
- 22 H. K. Kleinman and G. R. Martin, *Semin. Cancer Biol.*, 2005, **15**, 378–386.
- 23 J. Debnath, S. K. Muthuswamy and J. S. Brugge, *Methods*, 2003, **30**, 256–268.
- 24 M. M. P. Zegers, L. E. O'Brien, W. Yu, A. Datta and K. E. Mostov, *Trends Cell Biol.*, 2003, **13**, 169–176.
- 25 K. L. Sodek, T. J. Brown and M. J. Ringuette, *BMC Cancer*, 2008, **8**, 223.
- 26 O. D. Wever, A. Hendrix, A. D. Boeck, W. Westbroek, G. Braems, S. Emami, M. Sabbah, C. Gespach and M. Bracke, *Int. J. Dev. Biol.*, 2010, **54**, 887–896.
- 27 F. Taneri, O. Kurukahvecioglu, N. Akyurek, E. H. Tekin, M. N. İlhan, C. Ciftci, S. Bozkurt, A. Dursun, O. Bayram and E. Onuk, *Eur. Surg. Res.*, 2006, **38**, 545–549.
- 28 P. Schedin, *Nat. Rev. Cancer*, 2006, **6**, 281–291.
- 29 S. Oh, H. Ryu, D. Tahk, J. Ko, Y. Chung, H. K. Lee, T. R. Lee and N. L. Jeon, *Lab Chip*, 2017, **17**, 3405–3414.
- 30 S. Lee, S. Kim, J. Ahn, J. Park, B. Y. Ryu and J. Y. Park, *Biofabrication*, 2020, **12**, 045031.
- 31 D. Ahmed, C. Y. Chan, S. C. S. Lin, H. S. Muddana, N. Nama, S. J. Benkovic and T. J. Huang, *Lab Chip*, 2013, **13**, 328–331.
- 32 Y. Du, M. J. Hancock, J. He, J. L. Villa-Uribe, B. Wang, D. M. Cropek and A. Khademhosseini, *Biomaterials*, 2010, **31**, 2686–2694.
- 33 Y. Jiao and S. Torquato, *Phys. Biol.*, 2012, **9**, 036009.
- 34 E. H. Imen, M. Nakamura, M. Mie and E. Kobatake, *J. Biotechnol.*, 2009, **139**, 19–25.
- 35 E. Spitzer, R. Grosse, D. Kunde and H. E. Schmidt, *Int. J. Cancer*, 1987, **39**, 279–282.
- 36 T. L. Woodward, J. Xie, J. L. Fendrick and S. Z. Haslam, *Endocrinology*, 2000, **141**, 3578–3586.
- 37 U. Philippar, E. T. Roussos, M. Oser, H. Yamaguchi, H. D. Kim, S. Giampieri, Y. Wang, S. Goswami, J. B. Wyckoff, D. A. Lauffenburger, E. Sahai, J. S. Condeelis and F. B. Gertler, *Dev. Cell*, 2008, **15**, 813–828.
- 38 W. W. Du, L. Fang, M. Li, X. Yang, Y. Liang, C. Peng, W. Qian, Y. Q. O'Malley, R. W. Askeland, S. Sugg, J. Qian, J. Lin, Z. Jiang, A. J. Yee, M. Sefton, Z. Deng, S. W. Shan, C. H. Wang and B. B. Yang, *J. Cell Sci.*, 2013, **126**, 1440–1453.
- 39 H. S. Rasmussen and P. P. McCann, *Pharmacol. Ther.*, 1997, **75**, 69–75.
- 40 J. S. Yang, C. W. Lin, S. C. Su and S. F. Yang, *Expert Opin. Drug Metab. Toxicol.*, 2016, **12**, 191–200.
- 41 K. Ding, M. Gao, D. Lei, J. Luo, L. Zhang, X. Lu, Y. Zhang, Z. Zhang, Z. Tu, Y. Xu and X. Ren, *J. Med. Chem.*, 2013, **56**, 3281–3295.
- 42 Q. Lu, W. Chen, J. Peng, Y. Xu, Q. Cai, G. Feng, K. Ding, X. Zhu and Z. Guan, *Oncol. Lett.*, 2016, **12**, 3598–3608; A. Krtolica, C. O. D. Solorzano, S. Lockett and J. Campisi, *Cytometry*, 2002, **49**, 73–82.

- 43 A. Krtolica, C. O. D. Solorzano, S. Lockett and J. Campisi, *Cytometry*, 2002, **49**, 73–82.
- 44 T. A. McCaffrey, L. A. Agarwal and B. B. Weksler, *In Vitro Cell. Dev. Biol.*, 1988, **24**, 247–252.
- 45 Q. Fan, R. Liu, Y. Jiao, C. Tian, J. D. Farrell, W. Diao, X. Wang, F. Zhang, W. Yuan, H. Han, J. Chen, Y. Yang, X. Zhang, F. Ye, M. Li, Z. Ouyang and L. Liu, *Lab Chip*, 2017, **17**, 2852–2860.
- 46 D. Montandon, O. Kocher and G. Gabbiani, *Plast. Reconstr. Surg.*, 1982, **69**, 365–371.
- 47 R. Martinez-Orozco, N. Navarro-Tito, A. Soto-Guzman, L. Castro-Sanchez and E. P. Salazar, *Eur. J. Cell Biol.*, 2010, **89**, 476–488.
- 48 L. Castro-Sanchez, A. Soto-Guzman, M. Guaderrama-Diaz, P. Cortes-Reynosa and E. P. Salazar, *Clin. Exp. Metastasis*, 2011, **28**, 463–477.